Direct Visual Observation of Thermal Capillary Waves

Dirk G. A. L. Aarts,[1]* Matthias Schmidt,[2]†
Henk N. W. Lekkerkerker[1]

We studied the free fluid-fluid interface in a phase-separated colloid-polymer dispersion with laser scanning confocal microscopy and directly observed thermally induced capillary waves at the interface in real space. Experimental results for static and dynamic correlation functions validate the capillary wave model down to almost the particle level. The ultralow interfacial tension, the capillary length, and the capillary time are found to be in agreement with independent measurements. Furthermore, we show that capillary waves induce the spontaneous breakup of thin liquid films and thus are of key importance in the process of droplet coalescence.

At rest, the free interface between any two fluids, like that between a liquid and its vapor, appears to be smooth. Yet thermal motion inevitably gives rise to statistical fluctuations of the local interface position, leading to a rough interface. This phenomenon was first predicted by von Smoluchowski in 1908 (*1*); 5 years later, Mandelstam quantitatively described the interface roughness in terms of thermally excited capillary waves (*2*). These capillary waves have been studied with light (*3*) and x-ray scattering (*4*–*8*). They play an important role in modern theories of interfaces (*9*–*11*) and have been argued to be essential in the rupture of thin liquid films (*12*, *13*), as occurs in droplet coalescence. We show how to tune length and time scales with the use of colloidal suspensions, such that the fluctuating fluid-fluid interfaces can be seen directly in real space with a resolution comparable to the particle size. Moreover, the droplet coalescence event can be observed down to the scale of capillary fluctuations in quasi slow motion.

In the capillary wave spectrum, each Fourier component $h_{\mathbf{k}}$ of the interface displacement contributes according to the equipartition theorem

$$\langle |h_{\mathbf{k}}|^2 \rangle = \frac{k_B T}{\gamma L^2} \frac{1}{k^2 + \xi^{-2}} \qquad (1)$$

leading to an interface roughness proportional to $\sqrt{k_B T/\gamma}$. Here, γ is the interfacial tension between the two fluids, k_B is the Boltzmann constant, T is absolute temperature, L is the lateral system size, k is the absolute value of the wave vector $\mathbf{k}$, the angle brackets denote a thermal average, and ξ is the lateral correlation length (capillary length), defined as

$$\xi = \sqrt{\gamma/(g\Delta\rho)} \qquad (2)$$

where g is Earth's acceleration and $\Delta\rho$ is the mass density difference between the two phases. In molecular fluids, γ is on the order of 10 to 100 mN/m and $\Delta\rho$ is about 10^2 to 10^3 kg/m^3. Therefore, the interface roughness is ~0.3 nm, whereas the correlation length is ~3 mm, resulting in extreme roughness–correlation length ratios of 10^{-7}; such ratios are only accessible through scattering techniques. Here we exploit the scaling up of lengths when going from molecules to mesoscopic colloidal particles (diameter ~100 nm) to directly observe capillary waves in real space.

Adding polymer to a colloidal suspension may induce a fluid-fluid demixing transition that is widely accepted to be the mesoscopic analog of the liquid-gas phase transition in atomic substances (*14*). The coexisting phases are a colloidal liquid (rich in colloid and poor in polymer) and a colloidal gas (poor in colloid and rich in polymer). The origin of the phase separation lies in the entropy-driven attraction between the colloids, which is mediated by the polymers (*15*, *16*). It is known from experiment (*17*–*19*) and theory (*20*–*22*) that in such systems the interfacial tension scales as $\gamma \sim k_B T/d^2$, where d is the particle size, leading to ultralow values for γ (~1 μN/m and below). This in turn implies that using colloidal suspensions scales up the interface roughness and simultaneously scales down the correlation length. With the current system (see below), we successfully bring both into the μm regime. In addition, the interplay between ultralow interfacial tension and relatively large viscosity, η, sets the capillary velocity γ/η [see, e.g., (*23*)] in the range of μm/s, as opposed to typical velocities on the order of 10 m/s in molecular fluids. The associated characteristic time for the decay of interfacial fluctuations, which we refer to as the capillary time

$$\tau = \xi\eta/\gamma \qquad (3)$$

becomes on the order of seconds in the case of colloids. The capillary velocity also sets the time in droplet coalescence (*24*). Thus, through the appropriate choice of the colloid diameter, we can trace both the statics and dynamics of the capillary waves at a free interface and fully explore the coalescence events with optical microscopy.

We used fluorescently labeled poly(methylmethacrylate) (PMMA) colloidal spheres (*25*) with radius R_c = 71 nm (obtained from static light scattering) and size polydispersity of less than 10%. The polymer was commercially available polystyrene (Fluka) with molecular weight $M_w = 2 \times 10^6$ g mol^{-1} ($M_w/M_n < 1.2$, where M_n is number-average molecular weight) and radius of gyration R_g ~ 44 nm [estimated from data in the literature (*26*)]. Thus, the size ratio, $R_g/R_c = 0.6$, was sufficiently large to obtain stable fluid-fluid demixing (*27*). Both species were dispersed in cis/trans-decalin, and because all densities were known, mass fractions could be directly converted to packing fractions of colloids, $\phi_c = {}^4/_3\pi R_c^3 n_c$, and polymers, $\phi_p = {}^4/_3\pi R_g^3 n_p$, where n_c and n_p are the number densities of colloids and polymers, respectively. Samples were prepared by mixing colloid and polymer stock dispersions and diluting with decalin to control the overall packing fractions ϕ_c and ϕ_p. Large glass cuvettes (volume ~1 cm^3) with very thin cover glass walls (0.17 mm) were used. A confocal scanning laser head (Nikon C1) was mounted on a horizontally placed light microscope (Nikon Eclipse E400). Each measurement was done after 1 day of equilibration. We checked that the system was well equilibrated by following the recovery of intensity after bleaching a space region in the gas and/or liquid phase. The recovery appeared to be governed solely through diffusion of particles without any indications of drift (e.g., through convection). Data sets were acquired at many different state points following several dilution lines. The underlying phase diagram is shown in Fig. 1.

[1]Van't Hoff Laboratory, Debye Institute, Utrecht University, Padualaan 8, 3584 CH Utrecht, Netherlands. [2]Soft Condensed Matter, Debye Institute, Utrecht University, Princetonplein 5, 3584 CC Utrecht, Netherlands.

*To whom correspondence should be addressed. E-mail: d.g.a.l.aarts@chem.uu.nl

†On leave from Institut für Theoretische Physik II, Heinrich-Heine-Universität Düsseldorf, Universitätsstraße 1, D-40225 Düsseldorf, Germany.

Pictures such as those in Fig. 2 represent an intensity distribution of fluorescent light, $I(x, z, t)$ at a certain time t, with x the horizontal (along the interface) and z the vertical (opposite to gravity) components of the space vector. The microscope records the fluorescence of excited dye within the colloids, hence the colloid-rich (liquid) phase appears bright and the colloid-poor (gas) phase appears dark. $I(x, z, t)$ is a direct measure of the local and instantaneous distribution of colloidal particles and provides the starting point for a statistical analysis. Because of the finite resolution (*28*), we can access length scales of $\sim 2R_c$; we neglect effects induced by the finite time needed to scan each frame, and we take I as an instantaneous snapshot (justified by comparing the colloid self-diffusion time with the scanning time). Thus, the real-space pictures in Fig. 2 show the structure of a gas-liquid interface practically at the particle scale. We rely on the concept of a local interface between both phases. In the spirit of a Gibbs dividing surface, we define an interface position $h(x, t)$ such that in one column of vertical length L_z the total intensity can be written as

$$\int_0^{L_z} dz I(x, z, t) = I_{liq}(x)h(x, t) + I_{gas}(x)[L_z - h(x, t)] \quad (4)$$

where $I_{gas}(x)$ and $I_{liq}(x)$ are the average bulk intensities in the gas and liquid phase, respectively, and are taken to be functions of x to account for the microscope objective properties. In practice, integrals in the notation are sums over pixels, and we have checked that the results of the subsequent analysis do not depend sensitively on the precise definitions of I_{gas} and I_{liq}. The resulting "height" function $h(x)$ (yellow line in Fig. 2) describes the interface position quite accurately. From top to bottom in Fig. 2 we approach the critical point, and both the capillary waves and density fluctuations increase while the density (intensity) difference between the two phases decreases.

For each frame the average interface position is $\bar{h}(t) \equiv \langle h(x', t)\rangle$, in which the angle brackets denote averages over primed quantities. The time-dependent height-height correlation function is constructed as

$$g_h(x, t) = \langle [h(x', t') - \bar{h}(t')][h(x' + x, t' + t) - \bar{h}(t' + t)]\rangle \quad (5)$$

The corresponding static correlation function, $g_h(x) \equiv g_h(x, t = 0)$, is obtained (*5*) by Fourier-transforming Eq. 1 as

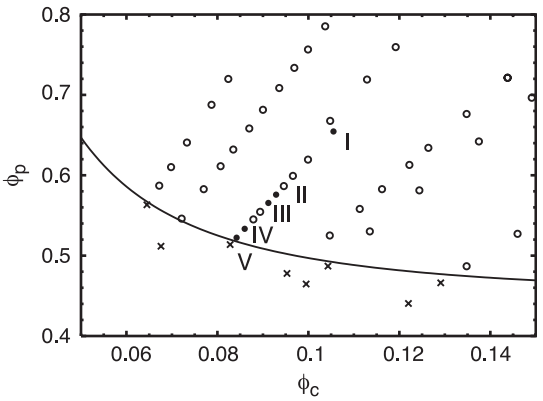

Fig. 1. Phase diagram in (ϕ_p, ϕ_c) representation. Indicated are state points where gas-liquid phase separation occurs (open and solid circles) and state points in the one-phase region (crosses). The line is an estimate of the binodal and is drawn to guide the eye. State points I to V (solid circles) are indicated.

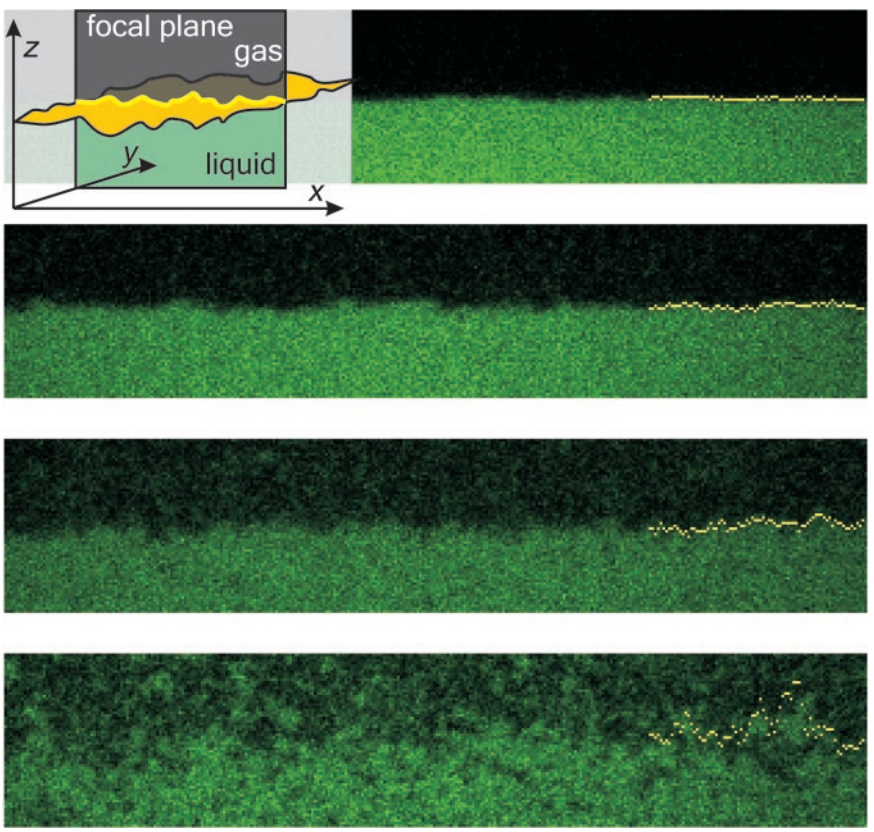

Fig. 2. Capillary waves at the free liquid-gas interface in a phase-separated colloid-polymer mixture imaged with laser scanning confocal microscopy (LSCM) at four different state points approaching the critical point (from top to bottom: state points I, III, IV, and V; see Fig. 1). The focal (viewing) plane is perpendicular to the interface, and only a very thin slice (thickness $\sim$0.6 μm) is imaged (see inset). Gravity points downward; each image is 17.5 μm by 85 μm. Thermally excited capillary waves corrugate the interface and their amplitude increases upon approaching the critical point. The yellow lines indicate the surface location $h(x)$ obtained with our method. See also movies S1 and S2 of the rough interfaces of state points III and IV.

$$g_h(x) = \frac{k_B T}{2\pi\gamma} K_0(x/\xi) \quad (6)$$

where K_0 is the modified Bessel function of the second kind as a function of x/ξ. Equation 6 holds for distances x larger than a small-distance cutoff on the order of the particle size. Capillary wave theory in the overdamped regime (*29*, *30*) predicts modes with wave vector $\mathbf{k}$ to decay according to $\exp[-t(\gamma k + g\Delta\rho/k)/\eta]$. Introducing $\bar{k} = \xi k$, the dynamical correlation function at fixed position, $g_h(t) \equiv g_h(x = 0, t)$, can be expressed as

$$g_h(t) = \frac{k_B T}{2\pi\gamma} \int_0^\infty d\bar{k}\, \bar{k}\, \frac{\exp[-(\bar{k} + \bar{k}^{-1})t/\tau]}{1 + \bar{k}^2} \quad (7)$$

where τ is as given in Eq. 3 with $\eta = \eta_{liq} + \eta_{gas}$, the sum of the viscosities of the (colloidal) liquid and gas phase (*29*, *30*).

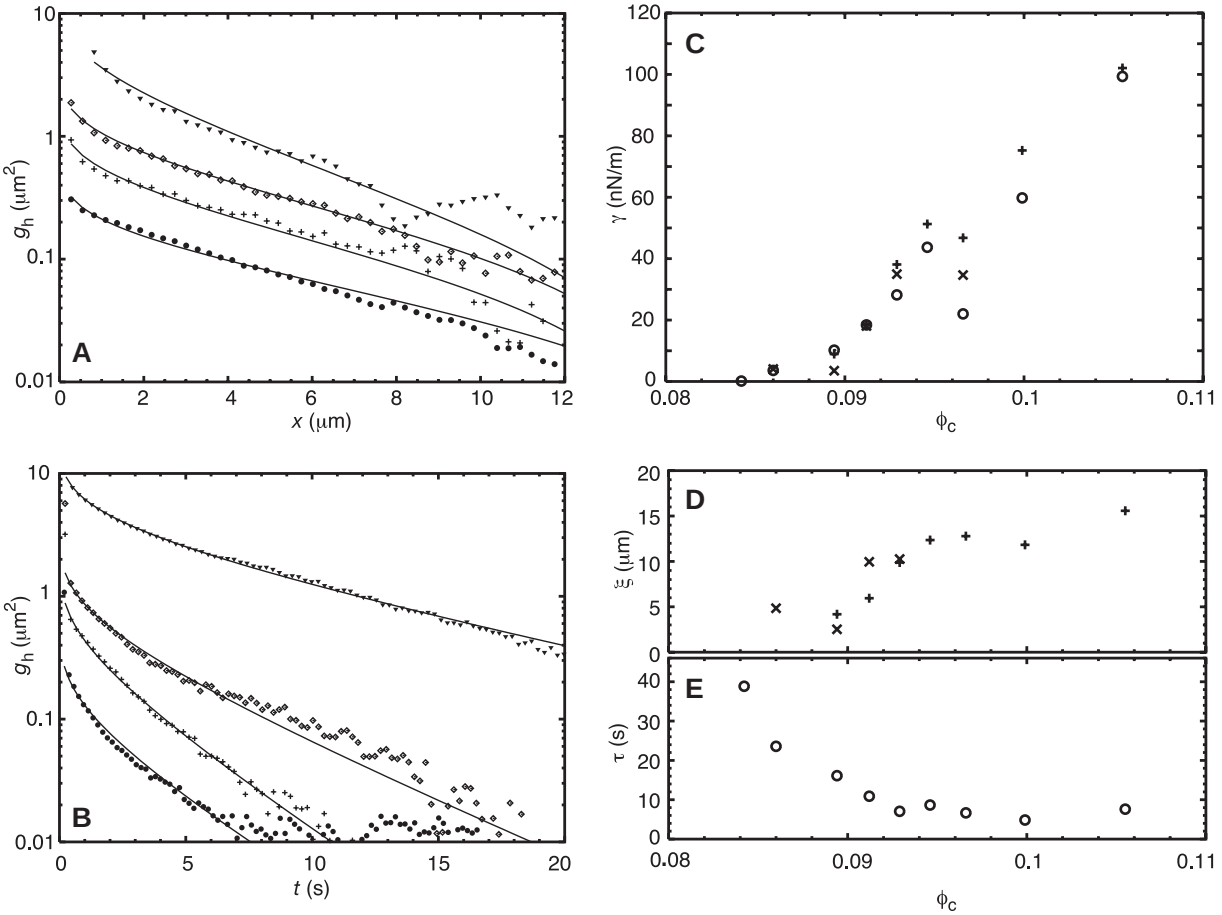

Fig. 3. Correlation functions characterizing the free (colloid) liquid-gas interface as obtained from quantitative analysis of LSCM pictures. (**A**) Static height-height correlation function $g_h(x)$ as a function of the (lateral) distance x for state points I, II, III, and IV (from bottom to top) approaching the critical point. Experimental results (symbols) are compared with predictions from the capillary wave model (lines). (**B**) Dynamical height-height correlation function at fixed position, $g_h(t)$, as a function of time t again for state points I to IV (from bottom to top). (**C**) Interfacial tension γ as a function of the overall colloid packing fraction ϕ_c obtained from $g_h(x)$ (crosses, slow frame rate; pluses, fast frame rate) and $g_h(t)$ (circles). (**D**) Capillary length ξ as a function of ϕ_c obtained from $g_h(x)$. (**E**) Capillary time τ as a function of ϕ_c obtained from $g_h(t)$. Results displayed in (C) to (E) stem from state points on the same dilution line as state points I to V.

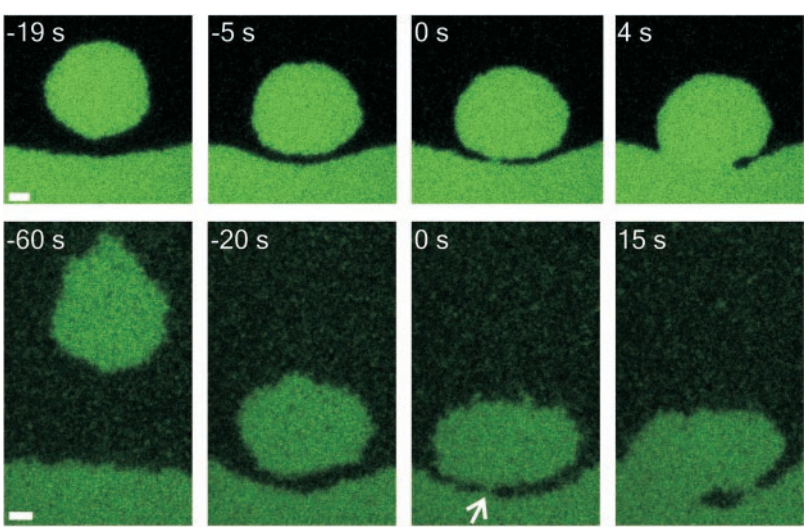

Fig. 4. Coalescence of colloidal liquid droplets with the bulk liquid phase. Occasionally, droplets that have condensed in the upper gas phase (during the final stages of phase separation) sediment toward the interface. The viewing setup is as shown in the inset of Fig. 2; scale bar, 5 μm. Top row, coalescence of a droplet of diameter ~16.5 μm for state point I (far away from the critical point); bottom row, coalescence of a droplet of diameter ~21.8 μm for state point IV (close to the critical point). The droplet surface is fluctuating and can be analyzed in a similar fashion as the planar interface. The three consecutive steps of the coalescence event can be followed in time (as indicated, where $t = 0$ corresponds to the instant of film breakup). Clearly, the capillary waves at both interfaces induce the breakup of the confined gas layer. In the series in the bottom row, the arrow denotes the place of film breakup. In this case, a second connection is made and the gas phase is being trapped in the liquid phase. See also movies S3 (corresponding to the top row) and S4 (corresponding to the bottom row) of these coalescence events.

Equations 6 and 7 describe the experimental data points very well, as can be clearly seen in Fig. 3, A and B, for various state points with only two physical parameters (γ, ξ in the static case and γ, τ in the dynamic case). Results for the interfacial tension, capillary length, and capillary time are displayed in Fig. 3, C to E, respectively. The relation of these quantities through Eq. 3 allows for an independent check of the consistency of our measurements. For example, for state point I, $\gamma = 100$ nN/m, $\xi = 15$ μm, and $\eta_{liq} + \eta_{gas} = (30 + 12.6)$ mPa·s, leading via Eq. 3 to a capillary time of 6 s. From the dynamical correlation function we find

$\tau = 7$ s. The quality of the fits and the internal agreement validate the capillary wave model down to the particle level.

The role of thermal capillary waves in droplet coalescence has long been a topic of speculation (*12*, *13*). The coalescence event is known to follow three steps: (i) film drainage of the continuous phase between the droplet and the free interface, (ii) breakup of the film, and (iii) extrusion of the droplet material into its bulk phase. Figure 4 displays these steps on the time and length scale of capillary fluctuations. We show two cases: that of a droplet far away from the critical point (top row of Fig. 4) and that of a droplet close to the critical point (bottom row of Fig. 4). In each row, the first and second panels show the drainage step, the third panel the film breakup, and the fourth panel the growth of the neck of the liquid bridge. The well-known Reynolds equation (*31*) describes the rate of thinning of the film (step 1) and the film drainage becomes very slow at small film thicknesses. The actual breakup of the film (step 2) is elusive in molecular fluids; here it is evident that capillary waves induce the spontaneous breakup, which occurs when two opposite bulges at the two interfaces meet. The probability for such an event depends on the interface roughness and on the interface correlation length and time. Typically, the connection is made at film thicknesses of $\sim$1 μm. A rough estimate shows that a fluctuation of 0.5 μm occurs in a couple of seconds. Hence, the breakup itself is a stochastic process dominated by capillary waves, but before and after the breakup, hydrodynamics apply. We observe that the neck of the liquid bridge (step 3) initially grows linearly with time. This initial regime is driven by the interfacial tension (*24*) and is extremely short in the case of molecular fluids because of the large capillary velocity, but in the present case the typical velocity is many orders of magnitude smaller. We thus see that the extremely low interfacial tension not only reveals the role of capillary waves in coalescence events, but also permits us to probe hydrodynamic regimes that were previously difficult to access in the laboratory.

References and Notes

1. M. V. von Smoluchowski, *Ann. Phys.* **25**, 205 (1908).
2. L. Mandelstam, *Ann. Phys.* **41**, 609 (1913).
3. A. Vrij, *Adv. Colloid Interface Sci.* **2**, 39 (1968).
4. M. K. Sanyal, S. K. Sinha, K. G. Huang, B. M. Ocko, *Phys. Rev. Lett.* **66**, 628 (1991).
5. M. Tolan *et al.*, *Phys. Rev. Lett.* **81**, 2731 (1998).
6. A. K. Doerr *et al.*, *Phys. Rev. Lett.* **83**, 3470 (1999).
7. C. Fradin *et al.*, *Nature* **403**, 871 (2000).
8. T. Seydel, A. Madsen, M. Tolan, G. Grübel, W. Press, *Phys. Rev. B* **63**, 073409 (2001).
9. F. P. Buff, R. A. Lovett, F. H. Stillinger, *Phys. Rev. Lett.* **15**, 621 (1965).
10. K. R. Mecke, S. Dietrich, *Phys. Rev. E* **59**, 6766 (1999).
11. A. Milchev, K. Binder, *Europhys. Lett.* **59**, 81 (2002).
12. A. Vrij, *Discuss. Faraday Soc.* **42**, 23 (1966).
13. A. Scheludko, *Adv. Colloid Interface Sci.* **44**, 391 (1967).
14. W. Poon, *J. Phys. Cond. Matter* **14**, R859 (2002).
15. S. Asakura, F. Oosawa, *J. Chem. Phys.* **22**, 1255 (1954).
16. A. Vrij, *Pure Appl. Chem.* **48**, 471 (1976).
17. E. H. A. de Hoog, H. N. W. Lekkerkerker, *J. Phys. Chem. B* **103**, 5274 (1999).
18. E. H. A. de Hoog, H. N. W. Lekkerkerker, *J. Phys. Chem. B* **105**, 11636 (2001).
19. D. G. A. L. Aarts, J. H. van der Wiel, H. N. W. Lekkerkerker, *J. Phys. Cond. Matter* **15**, S245 (2003).
20. A. Vrij, *Physica A* **235**, 120 (1997).
21. J. M. Brader, R. Evans, *Europhys. Lett.* **49**, 678 (2000).
22. J. M. Brader, R. Evans, M. Schmidt, H. Löwen, *J. Phys. Cond. Matter* **14**, L1 (2002).
23. R. F. Probstein, *Physicochemical Hydrodynamics* (Wiley, Hoboken, NJ, 2003), section 10.2.
24. J. Eggers, J. R. Lister, H. A. Stone, *J. Fluid Mech.* **401**, 293 (1999).
25. G. Bosma *et al.*, *J. Colloid Interface Sci.* **245**, 292 (2002).
26. B. Vincent, *Colloids Surf.* **50**, 241 (1990).
27. H. N. W. Lekkerkerker, W. C. K. Poon, P. N. Pusey, A. Stroobants, P. B. Warren, *Europhys. Lett.* **20**, 559 (1992).
28. T. Wilson, *Confocal Microscopy* (Academic Press, London, 1990).
29. J. Meunier, in *Liquids and Interfaces*, J. Charvolin, J. F. Joanny, J. Zinn-Justin, Eds. (North-Holland, New York, 1988), pp. 327–369.
30. U. S. Jeng, L. Esibov, L. Crow, A. Steyerl, *J. Phys. Cond. Matter* **10**, 4955 (1998).
31. O. Reynolds, *Philos. Trans. R. Soc. London* **177**, 157 (1886).

32. We thank D. Bonn, A. Petukhov, W. Kegel, A. van Blaaderen, and R. Dullens for useful discussions, and M. Dijkstra for her support. This work is part of the research program of the Stichting voor Fundamenteel Onderzoek der Materie (FOM) supported by the Nederlandse Organisatie voor Wetenschappelijk Onderzoek (NWO). Also supported by Deutsche Forschungsgemeinschaft SFB TR6.

Supporting Online Material

www.sciencemag.org/cgi/content/full/304/5672/847/DC1

Movies S1 to S4

23 February 2004; accepted 17 March 2004

RNA-Mediated Metal-Metal Bond Formation in the Synthesis of Hexagonal Palladium Nanoparticles

Lina A. Gugliotti, Daniel L. Feldheim,* Bruce E. Eaton*

RNA sequences have been discovered that mediate the growth of hexagonal palladium nanoparticles. In vitro selection techniques were used to evolve an initial library of $\sim 10^{14}$ unique RNA sequences through eight cycles of selection to yield several active sequence families. Of the five families, all representative members could form crystalline hexagonal palladium platelets. The palladium particle growth occurred in aqueous solution at ambient temperature, without any endogenous reducing agent, and at low concentrations of metal precursor (100 micromolar). Relative to metal precursor, the RNA concentration was significantly lower (1 micromolar), yet micrometer-size crystalline hexagonal palladium particles were formed rapidly (7.5 to 1 minutes).

Biomineralization achieves exquisite control over crystal type and hierarchical materials self-assembly with protein biopolymer templates. RNA molecules are also highly structured biopolymers. Given the landmark discovery of in vitro selection (*1*, *2*) and the use of these techniques to discover RNA catalysts that mediate a variety of organic reactions (*3–10*), we sought to determine whether RNA could serve as a template for inorganic–particle growth. Here we report examples of individual RNA sequences that mediate metal-metal bond formation to create novel inorganic materials.

Conventional methods for controlling metal-metal bond formation and crystal growth primarily use synthetic polymers. Archetypical examples are the formation of cubic silver and palladium particles using poly(acrylate) (*11*) or poly(vinylpyrollidone) templates (*12*). Smaller multidentate ligands such as trisodium citrate can be used to control crystal shape as well—for example, in the photoinduced conversion of silver nanospheres to triangular prisms (*13*).

In attempts to mimic natural biomineralization, proteins and polypeptides have been studied extensively as templates for materials synthesis (*14–17*). Belcher *et al.* have used phage display techniques to mine for peptides that can bind selectively to various semiconductor crystal faces (*18*). Knowledge of peptide-surface binding affinity was then used to engineer a virus that could bind and organize semiconductor nanocrystals into well-ordered thin-film assemblies (*19*). Much less research has focused on the interactions between materials

Department of Chemistry, North Carolina State University, Raleigh, NC 27695, USA.

*To whom correspondence should be addressed. E-mail: bruce_eaton@ncsu.edu (B.E.E.), dan_feldheim@ncsu.edu (D.L.F.)